

Article

Open Access



# A tiny amount of electrode additive breaks the dilemma of achieving high energy density and fast charging lithium-ion battery cathode

Jing Zhang<sup>1,2,#</sup>, Longhao Cao<sup>2,#</sup>, Jingxiong Yu<sup>2</sup>, Jie Gao<sup>2</sup>, Yingfeng Tu<sup>3</sup>, Ya-Jun Cheng<sup>2,4,\*</sup>, Wenwen Xue<sup>4,\*</sup>, Yonggao Xia<sup>2,5,\*</sup>, Yudai Huang<sup>1,\*</sup>

<sup>1</sup>State Key Laboratory of Chemistry and Utilization of Carbon Based Energy Resources; College of Chemistry, Xinjiang University, Urumqi 830017, Xinjiang, China.

<sup>2</sup>Ningbo Institute of Materials Technology & Engineering, Chinese Academy of Sciences, Ningbo 315201, Zhejiang, China.

<sup>3</sup>College of Chemistry, Chemical Engineering and Materials Science, Soochow University, Suzhou 215123, Jiangsu, China.

<sup>4</sup>College of Renewable Energy, Hohai University, Changzhou 213200, Jiangsu, China.

<sup>5</sup>Center of Materials Science and Optoelectronics Engineering, University of Chinese Academy of Sciences, Beijing 100049, China.

<sup>#</sup>Authors contributed equally.

**\*Correspondence to:** Prof. Ya-Jun Cheng, College of Renewable Energy, Hohai University, 1915 Hehai Avenue, Changzhou 213200, China. E-mail: chengyajun@hhu.edu.cn; Dr. Wenwen Xue, College of Renewable Energy, Hohai University, 1915 Hehai Avenue, Changzhou 213200, China. E-mail: 20241027@hhu.edu.cn; Prof. Yonggao Xia, Ningbo Institute of Materials Technology & Engineering, Chinese Academy of Sciences, 1219 Zhongguan West Rd, Ningbo 315201, China. E-mail: xiayg@nimte.ac.cn; Prof. Yudai Huang, State Key Laboratory of Chemistry and Utilization of Carbon Based Energy Resources; College of Chemistry, Xinjiang University, 777 Huarui Street, Urumqi 830017, China. E-mail: huangyd@xju.edu.cn

**How to cite this article:** Zhang, J.; Cao, L.; Yu, J.; Gao, J.; Tu, Y.; Cheng, Y. J.; Xue, W.; Xia, Y.; Huang, Y. A tiny amount of electrode additive breaks the dilemma of achieving high energy density and fast charging lithium-ion battery cathode. *Energy Mater.* 2025, 5, 500083. <https://dx.doi.org/10.20517/energymater.2024.224>

**Received:** 25 Oct 2024 **First Decision:** 7 Jan 2025 **Revised:** 21 Jan 2025 **Accepted:** 10 Feb 2025 **Published:** 21 Apr 2025

**Academic Editor:** Ho Seok Park **Copy Editor:** Ping Zhang **Production Editor:** Ping Zhang

## Abstract

It is crucial to achieve high energy density and fast charging simultaneously for automotive lithium-ion batteries. The nickel-rich layered oxide  $\text{LiNi}_{0.8}\text{Co}_{0.1}\text{Mn}_{0.1}\text{O}_2$  (NCM811) cathode enables high energy density due to its high theoretical capacity and high working voltage. However, the fast charging performance is compromised because the electrode-electrolyte interface kinetics deteriorates when working at high voltage. A new approach is proposed to solve this dilemma, where [60] Fullerenolacetic acid ( $\text{C}_{60}\text{-COOH}$ ) is used to tune the interface structure of the NCM811. The carboxylic acid functional group ensures preferential deposition of  $\text{C}_{60}$  onto the NCM811 surface through the reaction with the surface residual alkaline species/transition metals. An electronic and ionic conductive thin coating layer is formed on the NCM811 surface, which inhibits electrolyte decomposition and



© The Author(s) 2025. **Open Access** This article is licensed under a Creative Commons Attribution 4.0 International License (<https://creativecommons.org/licenses/by/4.0/>), which permits unrestricted use, sharing, adaptation, distribution and reproduction in any medium or format, for any purpose, even commercially, as long as you give appropriate credit to the original author(s) and the source, provide a link to the Creative Commons license, and indicate if changes were made.



facilitates formation of high voltage stable cathode electrolyte interface. With 0.50 wt.% of C<sub>60</sub>-COOH, the NCM811 cathode exhibits significantly improved electrochemical performance at 4.6 V in terms of reversible capacity, and capacity retention ratio, where an exceptional fast charging/discharging performance at 10 C is demonstrated as well. This work is of great significance for promoting high energy density and fast charging automotive lithium-ion batteries.

**Keywords:** Nickel-rich layered cathode, fullerene, high energy density, fast charging, lithium-ion battery

## INTRODUCTION

Lifting energy density and enhancing fast charging/discharging performance are two crucial aspects to promote automotive lithium-ion battery applications<sup>[1,2]</sup>. Nickel-rich layered cathode LiNi<sub>0.8</sub>Co<sub>0.1</sub>Mn<sub>0.1</sub>O<sub>2</sub> (NCM811) holds great promise to overcome both problems because the NCM811 cathode exhibits a high actual capacity and fast lithium ion transport between the layered structure<sup>[3,4]</sup>. Raising the charging voltage upper limit for NCM811 cathodes (for example, from 4.3 V to 4.6 V) is considered an effective way to increase the energy density. However, raising the voltage upper limit while maintaining fast charging/discharging performance is challenging. At high voltage, phase transitions from layered to spinel structure are extremely easy to occur, which destroys the structure of the cathode material and leads to a sharp reduction in reversible capacity<sup>[5]</sup>. Besides, high voltage can cause excessive side reactions on the cathode surface, forming an over-thick cathode electrolyte interface (CEI), leading to increased impedance and thus affecting the charging/discharging performance at high current density<sup>[6]</sup>. Surface modification with electron-conductive carbonaceous materials has been widely used to increase the energy density and improve rate performance of the NCM811 cathode. On the one hand, adverse side reactions are suppressed by the carbon coating at the electrode-electrolyte interface; on the other hand, polarization is reduced because the carbonaceous materials possess good electronic conductivity<sup>[7-9]</sup>. However, in the practical application of carbon coating in high nickel cathodes, because the transition metal (TM) ions of the NCM811 cathode are easily reduced during the sintering process, leading to structure collapse and performance deterioration<sup>[9,10]</sup>, the application effect of carbon coating is greatly limited.

In this work, [60] Fullerenooacetic acid (C<sub>60</sub>-COOH) is used to modify NCM811 particles; the schematic illustration is shown in [Figure 1](#). Because C<sub>60</sub>-COOH is soluble in organic solvents, a solution-based surface coating is possible. The functionalization with carboxylic acid group enhances interactions with the residual alkaline species/TMs at the NCM811 particle surface, thereby ensuring uniform and controllable deposition of C<sub>60</sub>-COOH onto the NCM811 particle surface. Fullerene has excellent electronic conductivity because of its unique molecular structure and electronic energy levels, which accelerates the transfer of active Li<sup>+</sup> at high current density, and promotes continuous adsorption of Li<sup>+</sup> and uniform deposition of CEI<sup>[11]</sup>. In addition, due to the multiple-addition of free radicals on a fullerene, fullerenes are regarded as highly efficient radical sponges; thus, they can protect the electrode by scavenging oxygen and related radicals. Based on this strategy and multiple mechanisms, without traditional and complex sintering process, directional deposition process and a tiny amount of additives break the dilemma of high-voltage and high-rate NCM811 cathodes, and the cathode particle surface is modified with an excellent reproducibility and promising scalability. Compared to the pristine NCM811 (P-NCM), the structure of the modified C-NCM cathode is stabilized; the electrochemical performance is improved.

## EXPERIMENTAL

### Preparation and assembly of cells

C<sub>60</sub>-COOH was synthesized following the procedure of references<sup>[12-14]</sup>, as shown in [Supplementary Figure 1](#). *tert*-Butyl [60] Fullerenooacetate was synthesized by the cyclopropanation of C<sub>60</sub> (99.9 %, Yongxin

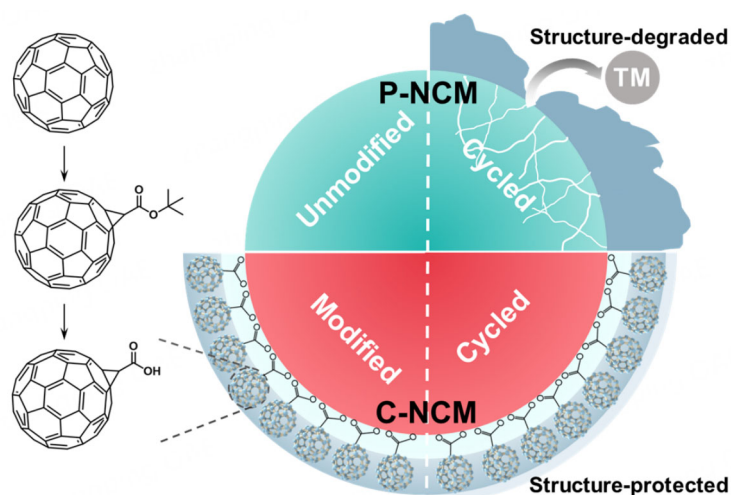


**Figure 1.** Working mechanism schemes of the pristine electrode P-NCM and the C<sub>60</sub>-COOH modified electrode C-NCM. C-NCM: C<sub>60</sub>-COOH modified NCM811; P-NCM: pristine NCM811.

Technology) with the sulfonium ylide prepared from *tert*-butyl bromoacetate and dimethyl sulfide, and readily converted to C<sub>60</sub>-COOH through the cleavage of the ester moiety promoted by trifluoroacetic acid. The total yield is 45%.

Firstly, prepare a mixed solution of N, N-dimethylformamide (DMF, 99.9%, Aladdin) and 1,2-dichlorobenzene (o-DCB, 99%, Aladdin) with a volume ratio of 1:1. Dissolve an appropriate amount of C<sub>60</sub>-COOH in a certain amount of mixed solution, add an appropriate amount of NCM811 (Neware, polycrystalline) powder, and control the mass of C<sub>60</sub>-COOH corresponding to 1 g of NCM811 to 0 mg, 0.25 mg, 0.50 mg, 0.75 mg, and 1.00 mg, respectively. Stir and react for 2 h, then spin evaporate and dry the resulting suspension to obtain NCM811 dry powder coated with different amounts of C<sub>60</sub> conductive network carbon.

The cathode consists of 80 wt.% active material (NCM811 coated with different amounts of C<sub>60</sub>-COOH), 10 wt.% conductive agent (TIMCAL Super C65), and 10 wt.% polyvinylidene fluoride binder (Solef PVDF5130). Dissolved them in a certain amount of 1-methyl-2-pyrrolidone (NMP, 99.9%, Aladdin) and mixed them to form a homogeneous slurry. Poured the mixed slurry onto aluminum foil, air drying at 60 °C for 2 h and vacuum drying at 110 °C for 12 h. The dried electrodes were pressed and cut into 14 mm diameter circle pieces for coin cells, or 80 × 44 mm<sup>2</sup> rectangles for pouch cells. The mass loadings of all cathodes for coin cells and pouch cells are about 3.5–4.0 mg·cm<sup>-2</sup> and 8.5 mg·cm<sup>-2</sup>, respectively.

The anode consists of 90 wt.% graphite (Neware), 3 wt.% conductive agent, 3 wt.% sodium carboxymethylcellulose (CMC, Daicel Corporation), and 3 wt.% styrene butadiene rubber (SBR, Daicel Corporation). Dissolved them in a quantity of deionized water and mixed them to form a homogeneous slurry. Poured the mixed slurry onto copper foil, air drying at 60 °C for 2 h and vacuum drying at 80 °C for 12 h. The dried electrodes were pressed and cut into 82 × 46 mm<sup>2</sup> rectangles for pouch cells. The N/P ratio of the control electrode is about 1.05: 1.

Transferred the electrodes to a glovebox filled with argon gas (O<sub>2</sub> < 0.5 ppm, H<sub>2</sub>O < 0.5 ppm) to assemble the 2032-coin cells and pouch cells. The half-cell used a lithium metal foil as a counter electrode and used

80  $\mu\text{L}$  electrolyte, and the pouch cell used a graphite electrode as a counter electrode and used 400  $\mu\text{L}$  electrolyte. The electrolyte consists of 1.0 mol  $\text{LiPF}_6$  dissolved in ethylene carbonate (EC)/dimethyl carbonate (DMC) (EC/DMC=3:7, by volume, Mitsui Chemicals). Celgard M825 was used as the separator. All graphite electrodes were not pre-lithiated before assembly.

### Electrochemical measurements

The assembled cells remained stationary overnight and were tested for their electrochemical performance at the LAND battery test system (Wuhan, China). For cycling testing, 1 C, 3 C, and 5 C cycle cells first undergo three charging/discharging cycles at 0.2 C and 0.5 C, respectively, followed by the remaining cycles (1 C = 200  $\text{mAh}\cdot\text{g}^{-1}$ ). The 10 C cycle cells first undergo two charging/discharging cycles at 0.2 C, 0.5 C and 1 C, respectively, followed by the remaining cycles. Cyclic voltammetry (CV) tests and electrochemical impedance spectroscopy (EIS) tests were performed on the Solartron analytical electrochemical workstation. The scanning rate for CV tests was 0.1  $\text{mV}\cdot\text{s}^{-1}$ . EIS measures applied a sine wave with an amplitude of 10.0 mV in the frequency range of 100 kHz to 0.01 Hz. The galvanized intermittent titration technique (GITT) experiment with a current pulse of 0.1 C for 30 min, followed by a standing time of 120 min. Unless otherwise specified, all cells shall be tested at 24  $^{\circ}\text{C}$  with a voltage of 2.8–4.6 V, characterized and analyzed using the 1 C cycling.

### Sample characterization

The field emission scanning electron microscope (FEI Quanta FEG 250, thermal field) equipped with an energy dispersive spectrometer (EDS, Oxford X-Max) characterized the elemental distribution on the electrode surface. The confocal micro-Raman spectroscopy (Renishaw in Via Reflex) studied the electrode surface state before and after cycling. The crystal structure of electrodes was analyzed using X-ray diffraction (XRD, Bruker D8 Discover), with a scanning range of  $5^{\circ}$  to  $90^{\circ}$ .

The cells to be characterized after cycling were disassembled in the glovebox, immersed in DMC for more than 5 h to remove residual lithium salts from the surface, and dried overnight in the glovebox. Field emission scanning electron microscopy (SEM, Hitachi S4800, cold field) was used to characterize the electrode surface morphology after cycling. High-resolution transmission electron microscope (HRTEM, JEOL2100) was used to characterize the CEI morphology and crystal structure of the electrode surface before and after cycling. The cross-sectional morphology of the electrode was characterized by focused ion beam SEM (FIB-SEM, Carl Zeiss/Auriga). X-ray photoelectron spectroscopy (XPS, Kratos Axis Supra) measurement was used to analyze the surface composition of the electrode after cycling. Thermogravimetric analysis-mass Spectroscopy (TG-MS) measurements were performed using the PerkinElmer TGA 8000 Spectrum two-Clarus SQ8T instrument. Place approximately 10 mg of delithium cathode (charged to 4.6 V) into an alumina crucible and transfer it to the instrument. Mass spectrometry was used to characterize gas production during the testing process from room temperature to 600  $^{\circ}\text{C}$  at a heating rate of 10  $^{\circ}\text{C}\cdot\text{min}^{-1}$  (nitrogen environment).

## RESULTS AND DISCUSSION

### The methodology and characterization

$\text{C}_{60}$ -COOH was synthesized following the protocol as references [Supplementary Figure 1]<sup>[12–14]</sup>, with the structure shown in Figure 2A. The transmission electron microscope (TEM) image of  $\text{C}_{60}$ -COOH powder exhibits uniform spherical particle shape as indicated in Figure 2B. The peak centered at 1,573  $\text{cm}^{-1}$  in the Raman spectra [Supplementary Figure 2] originates from the graphitic carbon structure, which enhances electronic conductivity and lithium-ion transport speed. The existence of  $\text{C}_{60}$ -COOH additive within the C-NCM cathode is confirmed by the characteristic  $\text{A}_{2g}$  and  $\text{E}_{2g}$  peaks displayed in the Raman spectra, which indicates that the graphitic carbon structure is well maintained. The profile distribution of C elements in the



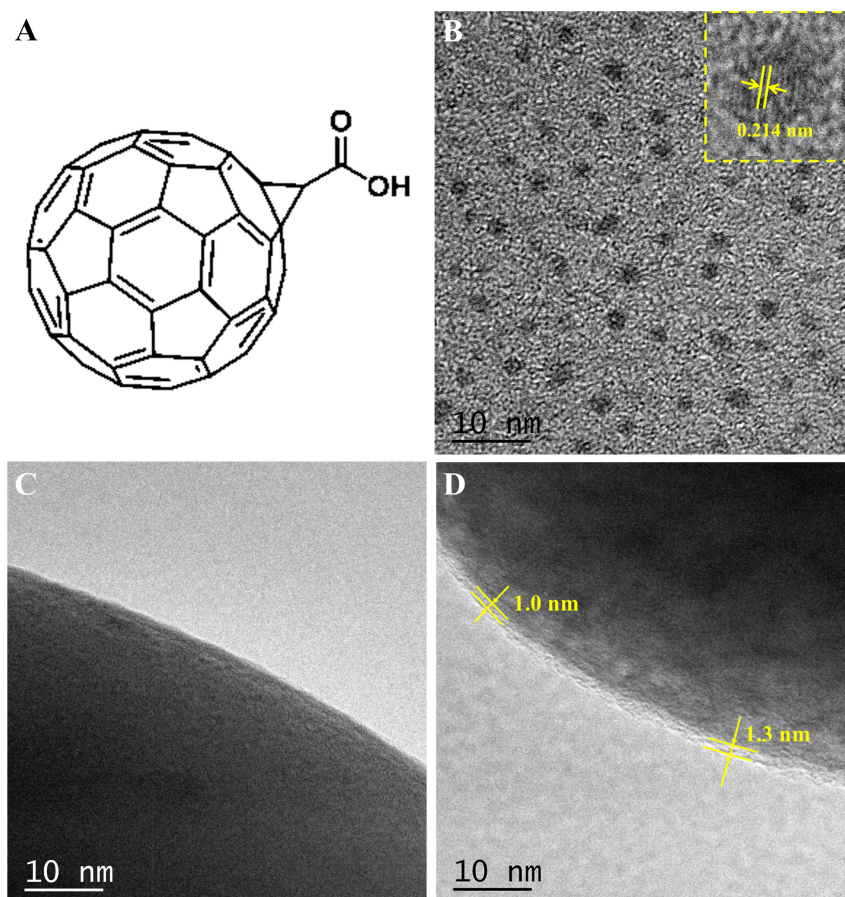


**Figure 2.** (A) Schematic illustration of [60] Fullerenenoacetic acid; (B) TEM image of [60] Fullerenenoacetic acid powder. TEM images of (C) P-NCM, and (D) C-NCM particles. TEM: Transmission electron microscope; C-NCM: C<sub>60</sub>-COOH modified NCM811; P-NCM: pristine NCM811.

energy dispersive X-ray (EDX) spectra is consistent with that of Ni, Co and Mn elements [Supplementary Figure 3], indicating the uniform distribution of C<sub>60</sub> additive on the surface of C-NCM particles. HRTEM in Figure 2C and D displays the surface morphology of P-NCM and C-NCM particles, where the surface of C-NCM particles is covered by a uniform thin interface film with a thickness of about 1.0–1.3 nm. In contrast, no such surface film on the surface of P-NCM particles, further demonstrating the C<sub>60</sub>-COOH has been uniformly deposited on the NCM811 surface. This is due to the good solubility and film-forming capability of C<sub>60</sub>-COOH, enabling uniform deposition on the surface of the cathode particle. The structure of P-NCM and C-NCM particles is also analyzed based on XRD patterns [Supplementary Figure 4], and lattice parameters are summarized in Supplementary Table 1. Both P-NCM and C-NCM particles retain the original space group (R3m), with a difference of approximately 0.1% in lattice parameters, and no impurity phase is detected, indicating that the surface treatment of C<sub>60</sub>-COOH does not cause any significant change in the crystal structure of NCM811 particles.

### Electrochemical performance

Different amounts of C<sub>60</sub>-COOH are used to modify the NCM811 surface in order to identify an optimal mass ratio with respect to the electrochemical performance improvement. In Supplementary Figure 5, the cycling performance is clearly influenced by the mass ratio of the C<sub>60</sub>-COOH additive to the NCM811 cathode. Compared with the pristine NCM811 (P-NCM), the NCM811 electrode modified with 0.50 wt.‰

C<sub>60</sub>-COOH (C-NCM-0.50) shows the best electrochemical performance. In contrast, the modified electrodes with alternative C<sub>60</sub>-COOH compositions (0.25 wt.% C<sub>60</sub>-COOH: C-NCM-0.25, 0.75 wt.% C<sub>60</sub>-COOH: C-NCM-0.75, 1.00 wt.% C<sub>60</sub>-COOH: C-NCM-1.00) do not show significant advantages. This is due to insufficient or excessive surface modification of C<sub>60</sub>-COOH, when the concentration of C<sub>60</sub>-COOH additives is too low, it is easy to cause uneven surface film formation and poor interface stability. When the C<sub>60</sub>-COOH additive concentration is too high, it is easy to cause the interface film to be too thick, hindering the diffusion of lithium ions, increasing the interface impedance and polarization, and causing the deterioration of interface kinetics. Therefore, a good balance between great electrode-electrolyte interface stability and limited interface impedance results in a significant improvement in the electrochemical performance of C-NCM-0.50 (abbreviated as C-NCM) compared to P-NCM electrodes. Based on the results, further studies are mainly addressed to the C-NCM in this manuscript unless specifically mentioned.

The rate performance of both samples is evaluated [Figure 3A]. It is found that the advantage of C-NCM is very limited at small current densities, while the performance is more favorable at large current densities. The long cycling performance of both samples at 10 C and a high voltage of 4.6 V [Supplementary Figure 6] is investigated. After 100 cycles, the discharge capacity of P-NCM and C-NCM is 45 mAh·g<sup>-1</sup> and 95 mAh·g<sup>-1</sup>, respectively. The significantly enhanced rate capacity indicates that better electrochemical kinetics is achieved with the C<sub>60</sub>-COOH additive to the NCM811. Meanwhile, we also tested the electrochemical performance of the two electrodes in high load [Supplementary Figure 7] and low temperature conditions [Supplementary Figure 8], and obtained the same results, which further proved the advantages of fullerenoacetic acid-modified cathodes, indicating that our research has universal applicability in high load and low temperature environment.

The effects of C<sub>60</sub>-COOH modification on NCM811 are further tested using the pouch cells [Figure 3B]. For C-NCM, the capacity is up to 153 mAh·g<sup>-1</sup> after 500 cycles, and the capacity retention ratio is 78.1%. In contrast, P-NCM has a low capacity (100 mAh·g<sup>-1</sup>) and decays rapidly (54.3%). The increased reversible capacity and enhanced capacity retention ratio of the NCM cathode in full cells are attributed to less active lithium loss and higher voltage plateau over cycles. The charging/discharging profile of P-NCM and C-NCM shows the first charge/discharge capacity of 241/201 mAh·g<sup>-1</sup> and 246/217 mAh·g<sup>-1</sup>, and first coulombic efficiency of 83.4% and 88.2% [Figure 3C], respectively. This improvement in first coulomb efficiency is attributed to the occurrence of lattice oxygen escape, accompanied by oxygen radical and O<sub>2</sub> evolution, at a charging voltage of higher than 4.5V<sup>[15,16]</sup>. The unique C<sub>60</sub>-COOH layer on the surface of C-NCM is capable of removing oxygen free radicals, prevents the oxygen species from reactions with carbonate electrolyte, and thus reduces irreversible capacity loss during the cycle<sup>[17]</sup>.

### Electrochemical kinetic analysis

The effect of C<sub>60</sub>-COOH additive on electrochemical kinetics is studied using CV [Supplementary Figure 9]. In the first cycle, the difference in redox peak potential of C-NCM is smaller (0.271 V) than that of P-NCM (0.315 V). It indicates that C-NCM has a lower polarization and faster reaction rate. The enhancement of electrochemical kinetics is attributed to the electronic and ionic conductive layer formed by C<sub>60</sub>. The surface C<sub>60</sub>-COOH layer enhances the affinity between the NCM811 particle and electronic conductive agent, which is beneficial for constructing electronic conductive network between particles.

The Li<sup>+</sup> diffusion behavior was characterized by GITT during the cycling process, where voltage variation and diffusion coefficient are functions of time [Figure 3D]. Since the voltage drop is caused by polarization in the stable state, the C<sub>60</sub>-COOH layer on the surface of C-NCM greatly inhibits the polarization, and the voltage drop is always less than or equal to P-NCM in a complete charging/discharging process. At the same

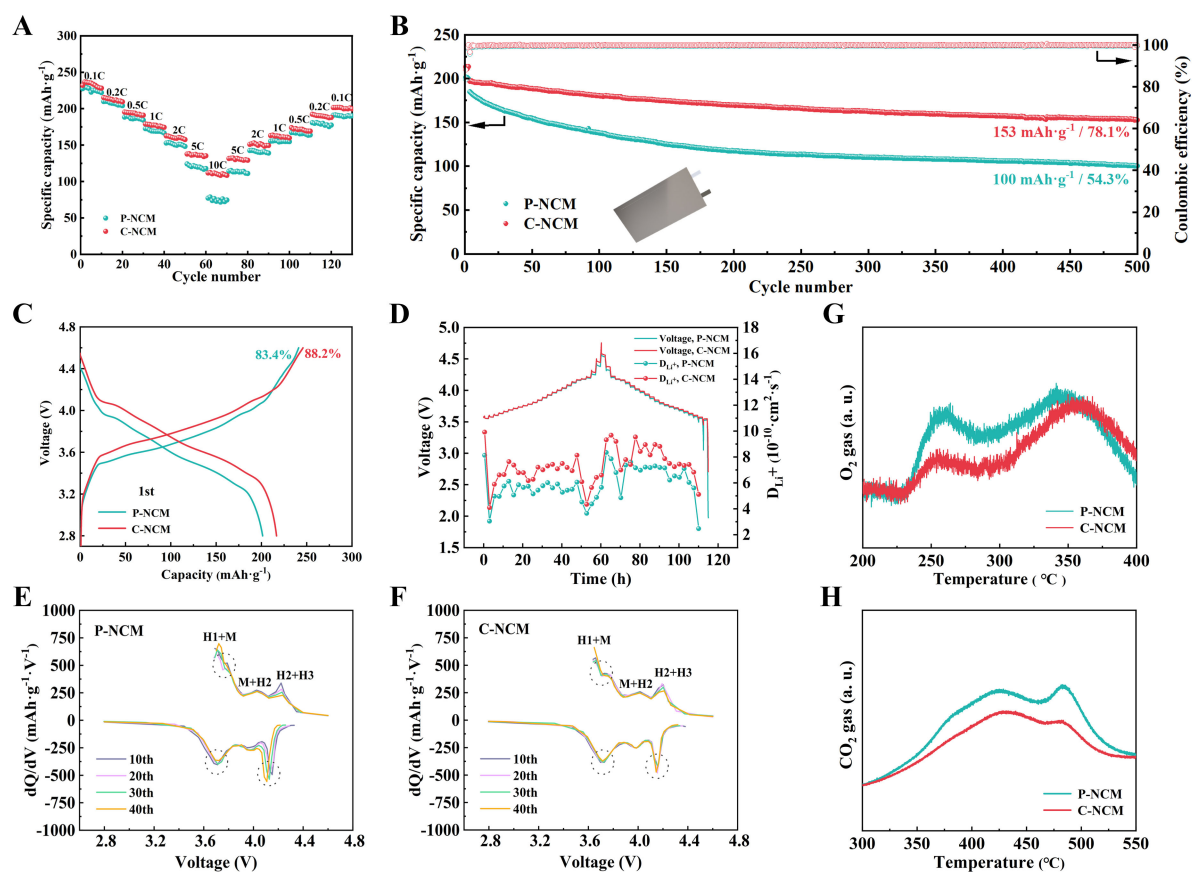


**Figure 3.** (A) Rate performance, (B) discharge capacities and coulombic efficiencies of pouch cells at 0.2 C; (C) initial charge/discharge profiles of pouch cells; (D) GITT profiles and Li<sup>+</sup> diffusion coefficient of both samples; dQ/dV profiles of (E) P-NCM and (F) C-NCM samples after cycles; (G) O<sub>2</sub> and (H) CO<sub>2</sub> release from both samples during heating process in the TG-MS testing. GITT: Galvanized intermittent titration technique; TG-MS: thermogravimetric analysis-mass spectroscopy; C-NCM: C<sub>60</sub>-COOH modified NCM811; P-NCM: pristine NCM811.

time, the average diffusion coefficient of C-NCM ( $7.3 \times 10^{-10} \text{ cm}^2 \cdot \text{s}^{-1}$ ) is always greater than that of P-NCM ( $5.9 \times 10^{-10} \text{ cm}^2 \cdot \text{s}^{-1}$ ) during a single charge/discharge, indicating that C<sub>60</sub>-COOH surface modification can effectively alleviate the electrode polarization under repeated current stimulation, leading to an increase in reversible capacity at high current densities.

It is reported that the cubic phase formed at a high cut-off voltage can inhibit the movement of Li<sup>+</sup>, resulting in an increase in charge transfer resistance, polarization and capacitance attenuation<sup>[5]</sup>. The EIS further confirm the enhanced electrochemical kinetics by the C<sub>60</sub>-COOH additive [Supplementary Figure 10 and Supplementary Table 2]. Compared to P-NCM, C-NCM shows that the interphase impedance is greatly suppressed. After 500 cycles, the R<sub>cei</sub> of C-NCM is 18.53 Ω, lower than that of P-NCM (21.77 Ω). This is due to the uncontrollable electrolyte decomposition on P-NCM surface and thick CEI with poor electronic and ion conductivity<sup>[18]</sup>. In contrast, due to the suppression of side reactions on the surface of C-NCM by the carbon layer, a thin and homogeneous CEI layer is formed. Therefore, the interface impedance of C-NCM is significantly suppressed.

The dQ/dV plots of both samples during the initial 40 cycles are analyzed to reveal the evolution of the polarization properties and the phase transition, as shown in Figure 3E and F. The oxidation peak of the

cycled P-NCM shifts toward high potential and the reduction peak shifts toward low potential during cycling, indicating an increased polarization<sup>[19,20]</sup>. In contrast, the peak shift observed in C-NCM is significantly smaller, and the excess potential is mitigated by the surface modification of the C<sub>60</sub> layer. In addition, due to the poor stability of the H3 phase, the H2 → H3 transition of P-NCM leads to significant contraction of the lattice c-axis, which further leads to anisotropic mechanical strain in the primary particles, and ultimately leading to the formation of intergranular micro-cracks and surface/interface damage<sup>[21,22]</sup>. The redox peak of C-NCM is well maintained, which further confirms that C<sub>60</sub>-COOH surface modification can effectively stabilize the CEI, reduce electrode polarization, and suppress the irreversible phase transition caused by Li<sup>+</sup> (de)intercalation.

### Thermal stability analysis

Another important factor to evaluate the applicability of the NCM811 at high voltages is thermal stability. The highly charged cathode surface undergoes a spinel and rock salt phase transition due to Ni migration at high temperatures. Large amount of hazardous gas is released, which further reacts with electrolyte to induce thermal runaway<sup>[23-25]</sup>. The thermal stability of both samples charged to 4.6 V is analyzed through TG-MS. Figure 3G and H shows the peak intensities of O<sub>2</sub> and CO<sub>2</sub> production at high temperatures, respectively. It can be found that the amount of O<sub>2</sub> and CO<sub>2</sub> produced by C-NCM is significantly reduced compared to those by P-NCM, and some of the peaks are even shifted towards higher temperatures. These results demonstrate that the C<sub>60</sub>-COOH layer can effectively stabilize NCM811 structure at high temperatures. The gas generation is inhibited and battery thermal safety is improved.

### Morphological and bulk structural analysis

The capacity attenuation of the high nickel layered oxide cathode is mainly due to its mechanical instability and high surface activity, especially at high state of charge (SOC). During repeated charging/discharging, anisotropic lattice distortion and volume change can lead to the accumulation of internal strain, eventually leading to crack formation or particle crushing<sup>[26]</sup>. Therefore, HRTEM and SEM are used to characterize the surface morphology of the cycled both samples. Figure 4A1-A4 shows the local structure of CEI on both electrode surfaces after 500 cycles. The CEI on P-NCM surface is not uniformly distributed with the thickness between 10-40 nm; the thick CEI layer leads to high interface resistance and hinders the diffusion of Li<sup>+</sup>. Additionally, the C-NCM surface exhibits a homogeneous and smooth CEI layer with a thickness of 5 nm. The thinner CEI layer enhances the electrochemical kinetics, and minimizes the decomposition of LiPF<sub>6</sub> on the cathode surface. The CEI layers formed on the different C-NCM show similar thicknesses, indicating that the growth of CEI layers is well controlled. The surface morphology of both electrodes is shown in Figure 4B1-B6, respectively. Severe cracks appeared on P-NCM electrode surface, and it is worth noting that when observing individual particle, these cracks also exist on the particle surface, indicating irreversible structural deformation during cycling. However, there are no significant cracks on the surface of C-NCM, and the particles remain intact. The cross-section morphology of both electrodes is studied by FIB-SEM [Figure 4C1-C2]. Figure 4C1 shows presence of cracks within P-NCM. The cracks propagate from the core region along the grain boundaries to the outside surface. The cracks are formed by the anisotropic lattice expansion and contraction of local grains at high voltage<sup>[2]</sup>. The cracks formed can provide space for electrolyte infiltration and uncontrolled growth of CEI layers, accompanied by increased impedance and irreversible phase transitions (H2-H3), leading to electrochemical kinetic delay and deterioration of cyclic stability<sup>[27]</sup>. However, only a few microcracks are observed within the C-NCM [Figure 4C2]. This indicates that the CEI derived from the C<sub>60</sub>-COOH layer stabilizes the bulk structure. In addition, even with a small number of cracks in NCM811, effective electron and ion transportation pathways are provided by the C<sub>60</sub>-COOH coating layer to prevent further surface degradation<sup>[9]</sup>.



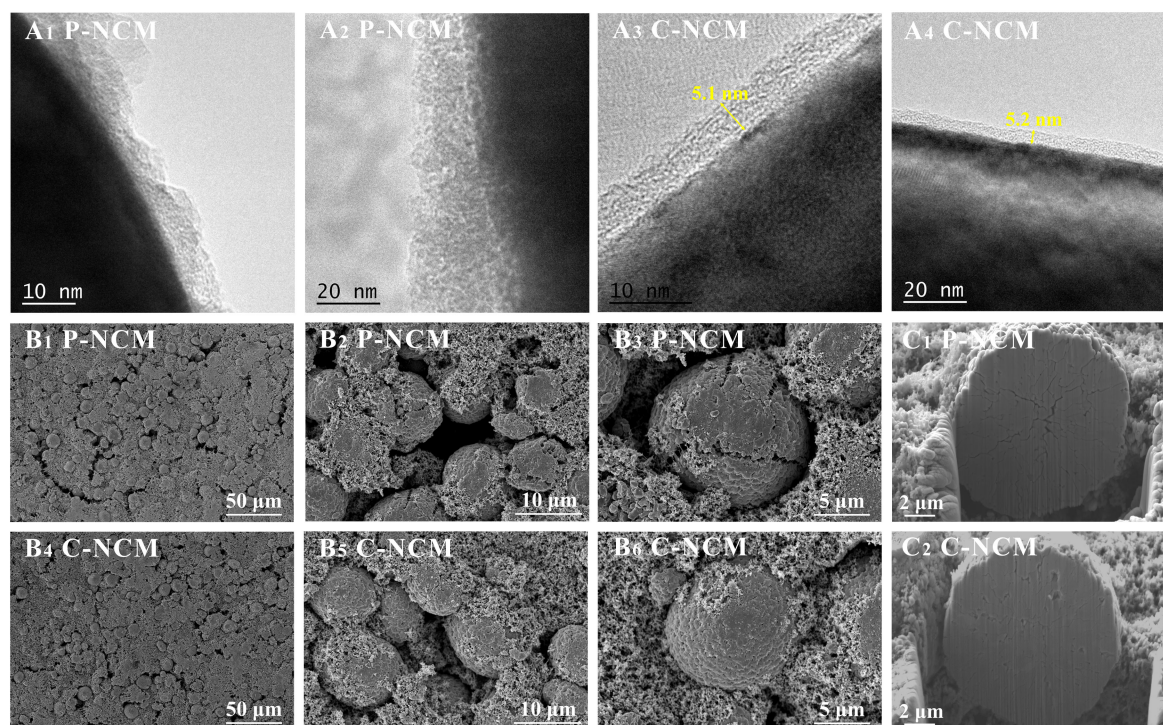


**Figure 4.** (A) HRTEM images of both electrodes after cycles; (B) Surface and (C) cross-section images of both electrodes after cycles. HRTEM: High-resolution transmission electron microscope.

The crystal structures of both samples after 500 cycles are visually demonstrated by a HRTEM coupled with fast Fourier transform (FFT) images [Figure 5]. The P-NCM particles exhibit blurry lattice fringes with some lattice distortion, and the corresponding FFT shows the presence of spinel phase (Fd3m). A lattice spacing of 0.206 nm is exhibited in the outer layer, consistent with the (400) crystal plane of the spinel phase. A lattice spacing of 0.480 nm is displayed in the inner layer, corresponding to the (111) crystal plane of the spinel phase. When cycling at 4.6 V, the strain caused by ion migration causes a transition from layered to spinel phase, which extends from the surface to the interior of the particles, and this phase transition is one of the main factors leading to the capacity attenuation and rate performance degradation of the cathode materials<sup>[28]</sup>. In contrast, the surface and bulk of C-NCM particles still exhibit a good hierarchical structure, with a well-defined and regular lattice in large area regions, without significant disorder domains. The FFT shows the lattice spacing of 0.472 nm, corresponding to the (003) crystal plane of the layered R3m phase. It has been shown that CEI derived from C<sub>60</sub>-COOH layer can stabilize the crystal structure on the surface and bulk and significantly improve its electrochemical properties.

XRD has been used to characterize the crystallographic phase change of both samples before and after 200 and 500 cycles. As shown in Figure 6A, all peaks in the XRD patterns of both samples exhibit a layered structure (R3m). The diffraction peaks of P-NCM significantly weaken and shift, indicating that the lattice parameters decrease with the deterioration of the cathode structure order, reflecting the loss of active lithium and the dissolution of TM during the cycle<sup>[29]</sup>. The peaks of (003), (101), and (104) reflect changes in the length of the c-axis, a-axis, and b-axis, respectively. After 500 cycles, the peak of (003) shifts towards the lower 2θ direction, indicating crystal expansion along the c-axis. Meanwhile, the strong electrostatic repulsion between the oxygen-oxygen interlayer due to active lithium loss yields an increased c-value<sup>[22,30]</sup>. The peak of (101) shifts towards the higher 2θ direction, indicating that the decrease of parameter a-axis is caused by the reduction of the length of Ni-O bond in the TMO<sub>6</sub> octahedron due to oxidation state during

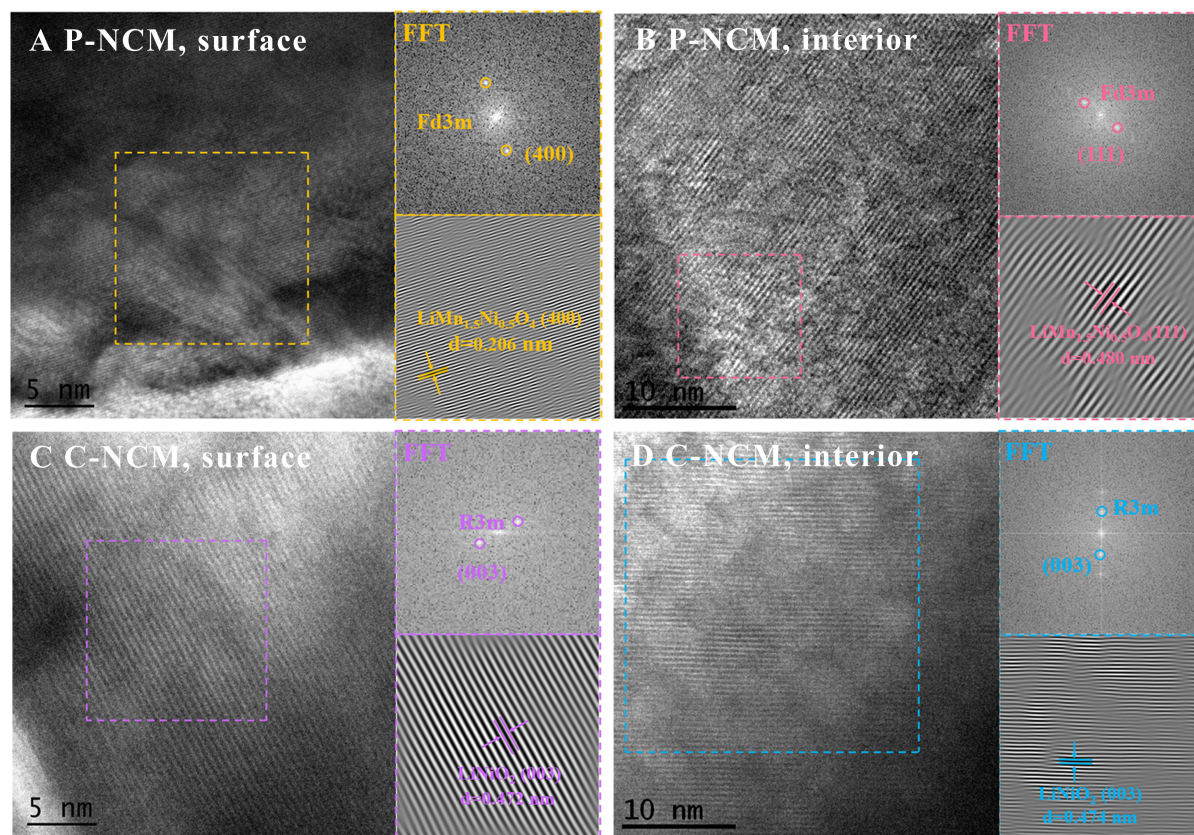


**Figure 5.** HRTEM images of the surface and interior of cathode particles of both samples after 500 cycles. HRTEM: High-resolution transmission electron microscope.

the cycle<sup>[31,32]</sup>. The peak of (104) shifts towards the higher 2θ direction, which is caused by the appearance of vacancies caused by the repeated (de)lithiation of  $\text{Li}^+$  in the lithium layer, and the occupation of these vacancies by  $\text{Ni}^{2+}$ <sup>[17]</sup>. In contrast, the peak shift and intensity reduction are smaller for C-NCM than those for P-NCM. This indicates that the CEI layer derived from  $\text{C}_{60}$ -COOH layer can effectively suppress phase transitions during charging and discharging, thereby improving the structure stability of NCM811.

Since XRD is difficult to characterize the surface spinel phase, Raman spectra were adopted for acquiring the surface structural information of both samples after 50, 100, 200, 500 cycles [Supplementary Figure 11]. In the Raman spectra, the transition rate from layered to spinel phase is significantly decelerated at the surface of C-NCM, especially after 200 cycles, due to the presence of the stable  $\text{C}_{60}$  layer. The combination of XRD and Raman characterization further proves that CEI derived from  $\text{C}_{60}$ -COOH layer can stabilize the TM ions on the particle surface, playing a crucial role in stabilizing the octahedral and layered structure of  $\text{TMO}_6$  during long-term cycling<sup>[33]</sup>. Raman spectra [Figure 6B] were also used to detect structural changes of the graphite anodes. After 500 cycles, the graphite anode corresponding to the P-NCM cathode exhibits a stronger D-band and a weaker G-band; this indicates that graphite structure corresponding to P-NCM cathode deteriorates, while forming more SEI species containing  $\text{sp}^3$  hybrid carbon<sup>[34]</sup>. The number of graphite structural defects is estimated by calculating the relative strength ratio between the D and G bands ( $R = I_D/I_G$ ). The high-degree structure disorder is indexed by a high R value<sup>[34]</sup>. With the  $\text{C}_{60}$ -COOH layer, the R-value of the graphite anode decreases from 0.1915 to 0.0908, indicating that the graphite anode corresponding to the C-NCM cathode maintains a better structural order. In addition, a new D'-band appearing at  $1614\text{ cm}^{-1}$  on the graphite anode corresponds to P-NCM cathode, indicating the presence of



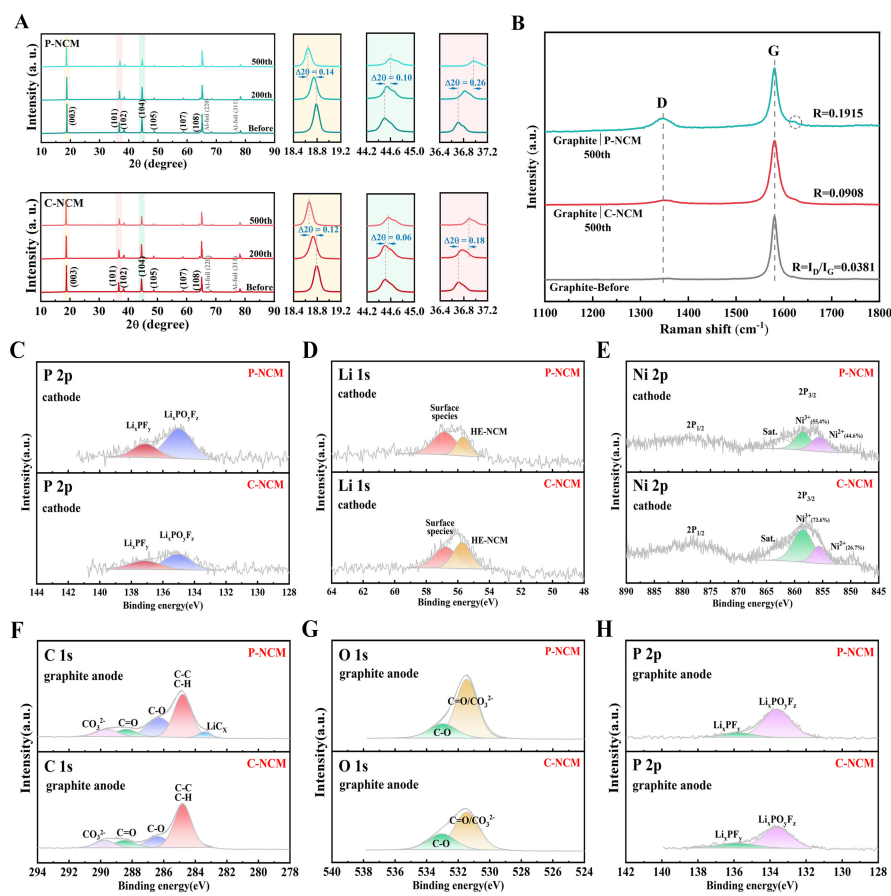


**Figure 6.** (A) XRD patterns and their local enlarged patterns of both samples before and after 200 and 500 cycles; (B) Raman spectra of graphite anodes relative to both cathodes without cycling and after 500 cycles; (C-E) XPS spectra of both samples after 500 cycles; (F-H) XPS spectra of graphite anodes relative to both samples after 500 cycles. XRD: X-ray diffraction; XPS: X-ray photoelectron spectroscopy.

oxidized  $\text{sp}^2$  carbon on the surface defects<sup>[31]</sup>. This further confirms the occurrence of structural disorder over cycles<sup>[35]</sup>. Due to the van der Waals force interaction between the atoms of a graphite anode, there is no chemical bonding, and the weak interaction between atoms makes it easy for large-volume solvent molecules to undergo intercalation reactions. The CEI derived from  $\text{C}_{60}$ -COOH on the cathode surface can effectively reduce the decomposition of the electrolyte, so the phenomenon of solvent molecules (such as  $\text{PF}_6^-$ ) embedded inside the lattice is significantly reduced in the electrochemical process of graphite anode<sup>[36]</sup>. Therefore, Raman spectra [Supplementary Figure 11 and Figure 6B] indicate that the  $\text{C}_{60}$ -COOH layer not only stabilizes the layered structure of NCM811, but also delays the structural degradation of the graphite anode.

### Element composition analysis

The composition of the electrode-electrolyte interface layer affects charge transportation. Therefore, the surface chemical composition of both cathodes [Figure 6C-E and Supplementary Figure 12] and their corresponding graphite anodes [Figure 6F-H and Supplementary Figure 13] after 500 cycles are investigated by XPS. In the C 1s spectra [Supplementary Figure 12A], C-NCM exhibits significantly more C-C/C-H peaks than P-NCM after cycling, indicating more C-C/C-H bonding from conductive carbon and PVDF. It means that the structure damage of the electrode during cycling is reduced. In the O 1s spectra [Supplementary Figure 12B], the peaks of C=O and C-O are attributed to electrolyte decomposition

products containing O element, and C-NCM exhibits reduced C-O peak, confirming the enrichment of fewer oxygen-containing species in CEI<sup>[6]</sup>. The decomposition of Lithium salt also plays a pivotal role in the formation of CEI in addition to the electrolyte. As shown in the F 1s [Supplementary Figure 12C] and P 2p [Figure 6C] spectra, the F 1s spectra consist of Metal-F, P-F, and C-F. Due to the migration of LiF between the cathode and anode during charging and discharging, the cathode cannot be effectively protected at high voltages<sup>[37]</sup>. In addition, LiF has a high ionic resistance and excess LiF increases the interfacial impedance<sup>[38,39]</sup>. Compared to P-NCM, the Li-F and P-F bonds on the C-NCM surface are significantly reduced, indicating that the CEI derived from the C<sub>60</sub>-COOH layer can effectively inhibit electrolyte decomposition and provide good protection for the cathode. This result corresponds to the peaks in the P 2p spectra of the Li<sub>x</sub>PF<sub>y</sub> and Li<sub>x</sub>PF<sub>y</sub>O<sub>z</sub> compounds. The Li 1s spectra [Figure 6D] show that the higher Li content in the bulk structure of C-NCM after cycling, and the fewer surface species, such as LiF, Li<sub>2</sub>CO<sub>3</sub>, ROCOOLi, etc.<sup>[40]</sup>. For the Ni 2p spectra [Figure 6E], the mixed valence states of Ni<sup>2+</sup> and Ni<sup>3+</sup> for both samples are shown. During the charging, the Ni<sup>4+</sup> formed by the removal of Li<sup>+</sup> is reduced to Ni<sup>3+</sup> or Ni<sup>2+</sup> due to Fluorine atom extraction from the derivatives of LiPF<sub>6</sub><sup>[41]</sup>. Moreover, oxygen release is required in the surface lattice accompanied with the reduction of surface Ni<sup>3+</sup> to Ni<sup>2+</sup> to maintain the charge neutrality of NCM811. Therefore, the decrease in Ni<sup>3+</sup> and increase in Ni<sup>2+</sup> at the cathode surface indicate the dissolution of Ni and the release of gas. On the P-NCM after the cycle, the Ni 2p<sub>1/2</sub> peak is no longer visible and the Ni 2p<sub>3/2</sub> peak is about to disappear, while the signal from C-NCM is still evident. Meanwhile, more Ni<sup>3+</sup> and less Ni<sup>2+</sup> in C-NCM indicate that the C<sub>60</sub>-COOH layer inhibits the formation of NiO-like rock salt phases by inhibiting the conversion of Ni<sup>3+</sup> to Ni<sup>2+</sup>, thus maintaining the crystal structure<sup>[42]</sup>. Overall, the XPS results of the cathode confirm that the uniform and ultra-thin CEI on the surface of the C-NCM electrode can inhibit the increase of resistance and the sharp decrease in capacity.

The XPS spectra in Figure 6F-H and Supplementary Figure 13 show the elemental composition on the surface of the graphite anode after 500 cycles. In the C 1s spectra [Figure 6F], it is worth noting that the peak of lithiated graphite species (LiC<sub>x</sub>) at 283.4 eV in the graphite electrode corresponding to P-NCM has special significance, which means that during the discharge process, some Li<sup>+</sup> are not fully removed from the graphite due to high overpotential<sup>[43,44]</sup>, resulting in a large loss of active lithium, corresponding to the results of the pouch full-cell cycle shown in Figure 3A. Compared to P-NCM, the spectra of O 1s [Figure 6G], F 1s [Supplementary Figure 13A], and P 2p [Figure 6H] show that graphite anodes corresponding to C-NCM have fewer C=O/CO<sub>3</sub><sup>2-</sup> and fewer F complexes and P compounds, which are decomposition products of electrolyte, such as carbonates and carboxylates<sup>[31]</sup>. The strong surface of Li compounds in the Li 1s spectra [Supplementary Figure 13B] and the strong Ni peak on the Ni 2p spectra [Supplementary Figure 13C] also indicate the formation of thick surface species on the graphite surface corresponding to P-NCM during the cycling process. These deposits impede the transport of Li<sup>+</sup> and lead to new side reactions with the electrolyte and increased interfacial resistance. In summary, the XPS results indicate that the C<sub>60</sub>-COOH modification produces the CEI layer inhibiting TM ion dissolution, migration and deposition. A compatible cathode/electrolyte interface is constructed with fast ion conductivity, thereby improving cycling performance in half-cell and pouch full-cell configurations.

## CONCLUSIONS

In order to solve the dilemma of achieving high energy density and fast charging performance of automotive lithium-ion batteries simultaneously, a simple and effective method is proposed to improve the performance of NCM811 cathodes at high voltage and high current densities. C<sub>60</sub>-COOH is introduced as an electrode additive to form a thin coating layer onto the NCM811 surface through the reaction with residual alkaline species/TMs. Due to efficient surface coating by the electronic and ionic conductive C<sub>60</sub>-COOH, only 0.50 wt.% of C<sub>60</sub>-COOH is needed to achieve a significantly improved electrochemical



performance of NCM811 in terms of reversible capacity and capacity retention ratio at 4.6 V, and rate performance at 10 C. The C<sub>60</sub>-COOH layer blocks direct contact between the electrolyte and electrode to construct a high voltage stable CEI layer. The cathode with fullerene modification yields fast charging performance by accelerating the electrochemical kinetics together with the thin inorganic-rich CEI layer. At the same time, because this work is based on the research of pouch cells, it has important practical significance for promoting the development of high energy density and fast charging lithium-ion batteries.

## DECLARATIONS

### Authors' contributions

Data curation, methodology: Zhang, J.; Cao, L.  
Investigation, validation: Zhang, J.; Cao, L.; Yu, J.  
Project administration: Gao, J.; Xue, W.; Huang, Y.  
Software: Zhang, J.; Yu, J.; Gao, J.  
Resources: Tu, Y.; Xue, W.; Xia, Y.  
Funding acquisition: Huang, Y.; Cheng, Y. J.  
Writing-original draft: Zhang, J.  
Writing- review and editing: Cheng, Y. J.; Huang, Y.

### Availability of data and materials

The data supporting our work can be found in the [Supplementary Materials](#).

### Financial support and sponsorship

This work was financially supported by the National Natural Science Foundation of China (52162036 and 22378342), the Key Project of Natural Science Foundation of Xinjiang Uygur Autonomous Region (2021D01D08), Key Laboratory Project Jointly Built by Xinjiang University (KFKT2022004), the Natural Science Foundation of Zhejiang Province (LD22E020003), the Ningbo Science & Technology Innovation 2025 Major Project (2023Z063), and Zhejiang Key Laboratory of Advanced Fuel Cells and Electrolyzers Technology.

### Conflicts of interest

All authors declared that there are no conflicts of interest.

### Ethical approval and consent to participate

Not applicable.

### Consent for publication

Not applicable.

### Copyright

© The Author(s) 2025.

## REFERENCES

1. Jiang, M.; Danilov, D. L.; Eichel, R.; Notten, P. H. L. A review of degradation mechanisms and recent achievements for Ni-rich cathode-based Li-ion batteries. *Adva. Energy. Mater.* **2021**, *11*, 2103005. [DOI](#)
2. Xu, C.; Reeves, P. J.; Jacquet, Q.; Grey, C. P. Phase behavior during electrochemical cycling of Ni-rich cathode materials for Li-ion batteries. *Adv. Energy. Mater.* **2021**, *11*, 2003404. [DOI](#)
3. Du, B.; Mo, Y.; Jin, H.; et al. Radially microstructural design of LiNi<sub>0.8</sub>Co<sub>0.1</sub>Mn<sub>0.1</sub>O<sub>2</sub> cathode material toward long-term cyclability and high rate capability at high voltage. *ACS. Appl. Energy. Mater.* **2020**, *3*, 6657-69. [DOI](#)
4. Han, J. G.; Kim, K.; Lee, Y.; Choi, N. S. Scavenging materials to stabilize LiPF<sub>6</sub>-containing carbonate-based electrolytes for Li-ion

- batteries. *Adv. Mater.* **2019**, *31*, e1804822. DOI
5. Liu, S.; Liu, Z.; Shen, X.; et al. Surface Doping to enhance structural integrity and performance of Li-rich layered oxide. *Adv. Energy Mater.* **2018**, *8*, 1802105. DOI
6. Han, J.; Hwang, C.; Kim, S. H.; et al. An antiaging electrolyte additive for high-energy-density lithium-ion batteries. *Adv. Energy Mater.* **2020**, *10*, 2000563. DOI
7. Hou, Q.; Cao, G.; Wang, P.; et al. Carbon coating nanostructured-LiNi<sub>1/3</sub>Co<sub>1/3</sub>Mn<sub>1/3</sub>O<sub>2</sub> cathode material synthesized by chemical vapor deposition method for high performance lithium-ion batteries. *J. Alloys. Compd.* **2018**, *747*, 796-802. DOI
8. Chen, X.; Ma, F.; Li, Y.; et al. Nitrogen-doped carbon coated LiNi<sub>0.6</sub>Co<sub>0.2</sub>Mn<sub>0.2</sub>O<sub>2</sub> cathode with enhanced electrochemical performance for Li-ion batteries. *Electrochim. Acta.* **2018**, *284*, 526-33. DOI
9. Hwang, J.; Do, K.; Ahn, H. Highly conductive 3D structural carbon network-encapsulated Ni-rich LiNi<sub>0.8</sub>Co<sub>0.1</sub>Mn<sub>0.1</sub>O<sub>2</sub> as depolarized and passivated cathode for lithium-ion batteries. *Chem. Eng. J.* **2021**, *406*, 126813. DOI
10. Noh, H.; Youn, S.; Yoon, C. S.; Sun, Y. Comparison of the structural and electrochemical properties of layered Li[Ni<sub>x</sub>Co<sub>y</sub>Mn<sub>z</sub>]O<sub>2</sub> (x = 1/3, 0.5, 0.6, 0.7, 0.8 and 0.85) cathode material for lithium-ion batteries. *J. Power. Sources.* **2013**, *233*, 121-30. DOI
11. Zhang, Y.; Li, J.; Tan, S.; et al. Fullerene-derivative C<sub>60</sub>-(OLi)<sub>n</sub> modified separators toward stable wide-temperature lithium metal batteries. *Chem. Eng. J.* **2022**, *446*, 137207. DOI
12. Zhang, X.; Hsu, C. H.; Ren, X.; et al. Supramolecular [60]fullerene liquid crystals formed by self-organized two-dimensional crystals. *Angew. Chem. Int. Ed.* **2015**, *54*, 114-7. DOI
13. Tada, T.; Ishida, Y.; Saigo, K. Synthesis and reactions of 2,2-[60]fullerenoalkanoyl chlorides. *J. Org. Chem.* **2006**, *71*, 1633-9. DOI PubMed
14. Lu, H.; Chen, X.; Li, X.; Sun, W.; Wang, Y.; Tu, Y. Effect of flexible spacer and alkyl tail length on the liquid crystalline phase behavior of fullerene block molecules. *Chemistry* **2023**, *29*, e202301015. DOI
15. Castel, E.; Berg, E. J.; El, K. M.; Novák, P.; Villevieille, C. Differential electrochemical mass spectrometry study of the interface of x Li<sub>2</sub>MnO<sub>3</sub>·(1 - x)LiMO<sub>2</sub> (M=Ni, Co, and Mn) material as a positive electrode in Li-ion batteries. *Chem. Mater.* **2014**, *26*, 5051-7. DOI
16. Hong, J.; Lim, H.; Lee, M.; et al. Critical role of oxygen evolved from layered Li-excess metal oxides in lithium rechargeable batteries. *Chem. Mater.* **2012**, *24*, 2692-7. DOI
17. Gan, Q.; Qin, N.; Zhu, Y.; et al. Polyvinylpyrrolidone-induced uniform surface-conductive polymer coating endows Ni-rich LiNi<sub>0.8</sub>Co<sub>0.1</sub>Mn<sub>0.1</sub>O<sub>2</sub> with enhanced cyclability for lithium-ion batteries. *ACS. Appl. Mater. Interfaces.* **2019**, *11*, 12594-604. DOI
18. Guo, F.; Xie, Y.; Zhang, Y. Tuning Li-excess to optimize Ni/Li exchange and improve stability of structure in LiNi<sub>0.8</sub>Co<sub>0.1</sub>Mn<sub>0.1</sub>O<sub>2</sub> cathode material for lithium-ion batteries. *Nano. Res.* **2022**, *15*, 8962-71. DOI
19. Park, K.; Jung, H.; Kuo, L.; Kaghazchi, P.; Yoon, C. S.; Sun, Y. Improved cycling stability of Li[Ni<sub>0.90</sub>Co<sub>0.05</sub>Mn<sub>0.05</sub>]O<sub>2</sub> through microstructure modification by boron doping for Li-ion batteries. *Adv. Energy Mater.* **2018**, *8*, 1801202. DOI
20. Zhang, J.; Li, J.; Cao, L.; et al. Surface-targeted functionalization of nickel-rich cathodes through synergistic slurry additive approach with multi-level impact using minimal quantity. *Nano. Res.* **2024**, *17*, 333-43. DOI
21. Liu, H.; Wolfman, M.; Karki, K.; et al. Intergranular cracking as a major cause of long-term capacity fading of layered cathodes. *Nano. Lett.* **2017**, *17*, 3452-7. DOI
22. Ni, L.; Chen, H.; Gao, J.; et al. Multiscale crystal field effect for high-performance ultrahigh-Ni layered cathode. *ACS. Nano.* **2023**, *17*, 12759-73. DOI
23. Wu, Y.; Liu, X.; Wang, L.; et al. Development of cathode-electrolyte-interphase for safer lithium batteries. *Energy. Storage. Mater.* **2021**, *37*, 77-86. DOI
24. Yi, M.; Dolocan, A.; Manthiram, A. Stabilizing the interphase in cobalt-free, ultrahigh-nickel cathodes for lithium-ion batteries. *Adv. Funct. Mater.* **2023**, *33*, 2213164. DOI
25. Kim, N.; Moon, J.; Ryou, M.; et al. Amphiphilic bottlebrush polymeric binders for high-mass-loading cathodes in lithium-ion batteries. *Adv. Energy Mater.* **2022**, *12*, 2102109. DOI
26. Li, J.; Manthiram, A. A Comprehensive analysis of the interphasial and structural evolution over long-term cycling of ultrahigh-nickel cathodes in lithium-ion batteries. *Adv. Energy Mater.* **2019**, *9*, 1902731. DOI
27. Zheng, Y.; Chen, L.; Su, Y.; et al. An interfacial framework for breaking through the Li-ion transport barrier of Li-rich layered cathode materials. *J. Mater. Chem. A.* **2017**, *5*, 24292-8. DOI
28. Gu, M.; Belharouak, I.; Zheng, J.; et al. Formation of the spinel phase in the layered composite cathode used in Li-ion batteries. *ACS. Nano.* **2013**, *7*, 760-7. DOI
29. He, J.; Melinte, G.; Darma, M. S. D.; et al. Surface structure evolution and its impact on the electrochemical performances of aqueous-processed high-voltage spinel LiNi<sub>0.5</sub>Mn<sub>1.5</sub>O<sub>4</sub> cathodes in lithium-ion batteries. *Adv. Funct. Mater.* **2022**, *32*, 2207937. DOI
30. Xie, Q.; Li, W.; Manthiram, A. A Mg-doped high-nickel layered oxide cathode enabling safer, high-energy-density Li-ion batteries. *Chem. Mater.* **2019**, *31*, 938-46. DOI
31. Pham, H. Q.; Mirolo, M.; Tarik, M.; El, K. M.; Trabesinger, S. Multifunctional electrolyte additive for improved interfacial stability in Ni-rich layered oxide full-cells. *Energy. Storage. Mater.* **2020**, *33*, 216-29. DOI
32. Qian, R.; Liu, Y.; Cheng, T.; et al. Enhanced surface chemical and structural stability of Ni-rich cathode materials by synchronous lithium-ion conductor coating for lithium-ion batteries. *ACS. Appl. Mater. Interfaces.* **2020**, *12*, 13813-23. DOI
33. Li, S.; Yang, L.; Liu, Z.; et al. Surface Al-doping for compromise between facilitating oxygen redox and enhancing structural stability of Li-rich layered oxide. *Energy. Storage. Mater.* **2023**, *55*, 356-63. DOI

34. Tang, Y.; Deng, J.; Li, W.; et al. Water-soluble sericin protein enabling stable solid-electrolyte interphase for fast charging high voltage battery electrode. *Adv. Mater.* **2017**, *29*. DOI
35. Zhang, J.; Li, Q.; Wang, Y.; Zheng, J.; Yu, X.; Li, H. Dynamic evolution of cathode electrolyte interphase (CEI) on high voltage LiCoO<sub>2</sub> cathode and its interaction with Li anode. *Energy. Storage. Mater.* **2018**, *14*, 1-7. DOI
36. Syzdek, J.; Marcinek, M.; Kostecki, R. Electrochemical activity of carbon blacks in LiPF<sub>6</sub>-based organic electrolytes. *J. Power. Sources.* **2014**, *245*, 739-44. DOI
37. Mu, P.; Zhang, H.; Jiang, H.; et al. Bioinspired antiaging binder additive addressing the challenge of chemical degradation of electrolyte at cathode/electrolyte interphase. *J. Am. Chem. Soc.* **2021**, *143*, 18041-51. DOI
38. Rong, H.; Xu, M.; Zhu, Y.; et al. A novel imidazole-based electrolyte additive for improved electrochemical performance of high voltage nickel-rich cathode coupled with graphite anode lithium ion battery. *J. Power. Sources.* **2016**, *332*, 312-21. DOI
39. Shi, X.; Zheng, T.; Xiong, J.; Zhu, B.; Cheng, Y. J.; Xia, Y. Stable electrode/electrolyte interface for high-voltage NCM 523 cathode constructed by synergistic positive and passive approaches. *ACS. Appl. Mater. Interfaces.* **2021**, *13*, 57107-17. DOI
40. Wu, Z.; Xue, L.; Ren, W.; Li, F.; Wen, L.; Cheng, H. A LiF nanoparticle-modified graphene electrode for high-power and high-energy lithium ion batteries. *Adv. Funct. Mater.* **2012**, *22*, 3290-7. DOI
41. Chen, Z.; Kim, G.; Chao, D.; et al. Toward greener lithium-ion batteries: aqueous binder-based LiNi<sub>0.4</sub>Co<sub>0.2</sub>Mn<sub>0.4</sub>O<sub>2</sub> cathode material with superior electrochemical performance. *J. Power. Sources.* **2017**, *372*, 180-7. DOI
42. Li, L.; Fu, L.; Li, M.; et al. B-doped and La<sub>4</sub>NiLiO<sub>8</sub>-coated Ni-rich cathode with enhanced structural and interfacial stability for lithium-ion batteries. *J. Energy. Chem.* **2022**, *71*, 588-94. DOI
43. He, M.; Su, C.; Feng, Z.; et al. High voltage LiNi<sub>0.5</sub>Mn<sub>0.3</sub>Co<sub>0.2</sub>O<sub>2</sub>/graphite cell cycled at 4.6 V with a FEC/HFDEC-based electrolyte. *Adv. Energy. Mater.* **2017**, *7*, 1700109. DOI
44. Beltrop, K.; Klein, S.; Nölle, R.; et al. Triphenylphosphine oxide as highly effective electrolyte additive for graphite/NMC811 lithium ion cells. *Chem. Mater.* **2018**, *30*, 2726-41. DOI